CIRP Annals - Manufacturing Technology 68 (2019) 53–56

Contents lists available at ScienceDirect

CIRP Annals - Manufacturing Technology

journal homepage: http://ees.elsevier.com/cirp/default.asp

Chip morphology and surface integrity in ultraprecision cutting of yttria-stabilized tetragonal zirconia polycrystal

Jiwang Yan (2)*, Takumi Okuuchi

Department of Mechanical Engineering, Keio University, Yokohama 223-8522, Japan

ARTICLE INFO

Keywords:
Surface integrity
Machinability
Micro machining

ABSTRACT

Yttria-stabilized tetragonal zirconia polycrystal (Y-TZP) is an important material for dental, biomedical, and mechanical applications. In this study, Y-TZP was cut by a single-crystal diamond tool in the micro-nanometre scale. The chip morphology and machined surface/subsurface properties under various conditions were investigated by scanning electron microscopy, Raman spectroscopy and cross-sectional transmission electron microscopy. Two factors dominating the material removal were identified: (i) crystal grain refinement and (ii) tetragonal-to-monoclinic phase transformation, the mechanisms of which were established by experiments and finite element simulations. This study provides a possible solution to the rapid fabrication of small 3D features on Y-TZP with nanometric surface roughness and an ultra-fine-grained subsurface layer.

1. Introduction

Yttria-stabilized tetragonal zirconia polycrystal (Y-TZP) is a fine ceramic material having excellent properties, such as high hardness, stiffness, chemical stability, and aesthetic effects. Due to these characteristics, Y-TZP has become an important material for dental restoration, biomedical components, sensors, optical fibre connectors, and so on. Grinding has been used for machining Y-TZP [1,2], but it is difficult for grinding to create small 3D features. In recent years, thermally assisted cutting of Y-TZP has been attempted by using tungsten carbide and cubic boron nitride tools [3,4]. However, the surface quality is low due to the unevenness of tool edge and possible thermal damage to sample surface. Thus far, there is no literature on the ultraprecision cutting of Y-TZP where the resulting surface roughness is in the nanometre regime.

In this study, a single-crystal diamond tool has been used to cut Y-TZP at the micro-nanometre scale to explore the feasibility of generating ultraprecision 3D features on Y-TZP with superior surface and subsurface quality. The chip morphology, surface topography, cutting force, subsurface damage, and tool wear have been investigated through both experiments and finite element (FE) simulations. This study will not only clarify the physics underlying Y-TZP machining but also provide guidelines for developing industrial processes such as diamond end milling.

2. Material and methods

Tetragonal zirconia polycrystal doped with yttria (Y_2O_3) at a concentration of 3 mol% was used as the workpiece. The grain size was ~300 nm, and density was 6.05 g/cm^3. The hardness, Young's modulus, and fracture toughness were 12.5 GPa, 210 GPa, and 6.0 MPam$^{1/2}$, respectively. The sample measured 23 × 23 × 5 mm^3, and its surface was polished before cutting.

The cutting experiment was carried out on a three-axis control ultraprecision lathe ASP-15 (Nachi-Fujikoshi Corp., Japan). The machine had a hydrostatic bearing spindle, a hydrostatic rotary table, and two hydrostatic linear tables. The resolution of the linear tables was 1 nm per step. A single-crystal diamond tool with a nose radius of 1.0 mm, rake angle of 0°, relief angle of 8°, and estimated edge radius of ~50 nm was used for cutting.

To obtain a high cutting speed over the small workpiece surface, diamond turning was carried out by fixing the workpiece to the spindle end at an offset of ~50 mm from the spindle centre. The spindle rotation rate was adjusted to keep the cutting speed constant at 50 m/min for all the tests. A piezoelectric dynamometer Kistler 9256C2 was used to measure cutting forces. Fig. 1 shows a schematic model of diamond turning with a round-nosed diamond tool, where the maximum undeformed chip thickness h_{max} can be calculated by Eq. (1):

$$h_{max} = R - \sqrt{R^2 + f^2 - 2f\sqrt{2Rd - d^2}} \quad (1)$$

where R is the tool nose radius, f the feed rate, and d the depth of cut. In this study, h_{max} was varied from ~1 μm to ~50 nm by changing f from 10 to 0.5 μm/rev at a constant d of 5 μm. In order to collect cutting chips, the experiments were conducted under dry conditions.

3. Results

3.1. Surface topography

Fig. 2 shows scanning electron microscopy (SEM) images of the machined surface of Y-TZP. When $f > 2$ μm/rev, microfractures and

* Corresponding author.
E-mail address: yan@mech.keio.ac.jp (J. Yan).

https://doi.org/10.1016/j.cirp.2019.04.050
0007-8506/

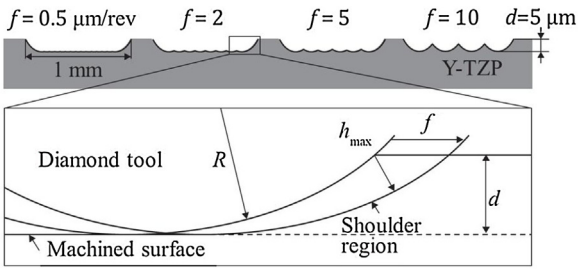

Fig. 1. Schematic of diamond turning with a round-nosed tool.

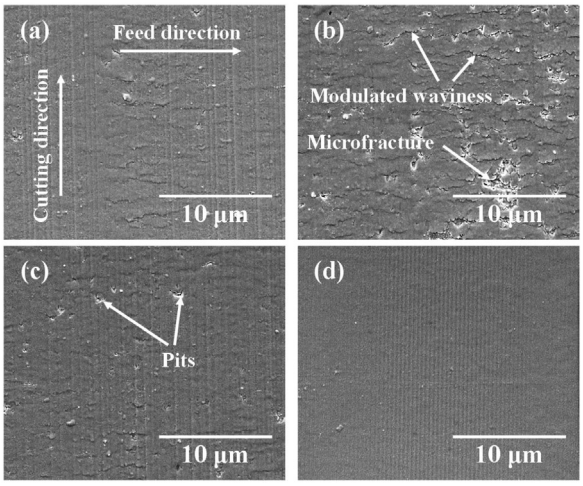

Fig. 2. SEM images of the machined surface obtained when: (a) $f = 10$, (b) $f = 5$, (c) $f = 2$, and (d) $f = 0.5\,\mu$m/rev.

micro pits due to grain dislodgements were found on the surface (Fig. 2(a)–(c)). In addition, modulated waviness perpendicular to the cutting direction was observed. The modulated waviness was especially significant at f = 5 μm/rev (Fig. 2(b)), which might be a result of the stick-slip phenomenon occurring at the interface of the tool and workpiece. At f = 0.5 μm/rev, however, uniform tool feed marks appeared while no microfractures, pits, or modulated waviness were observed on the surface (Fig. 2(d)).

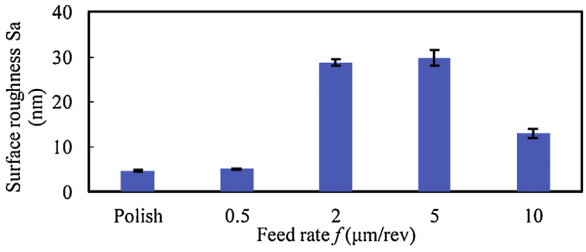

Fig. 3. Variation in surface roughness with tool feed rate.

The variation in surface roughness with tool feed rate is shown in Fig. 3. When $f > 2$ μm/rev, surface roughness Sa was higher than 10 nm due to the occurrence of microfractures, micro pits, and modulated waviness. At a feed rate of 0.5 μm/rev, however, the surface roughness was 5 nm Sa, which is almost as smooth as the polished surface (4 nm Sa).

3.2. Chip morphology

Fig. 4 shows SEM images of cutting chips obtained at various tool feed rates. The chips are generally continuous under all conditions, indicating that plastic deformation has dominated the material removal of Y-TZP at the micro-nanometre scale. However, cracks were observed at the chip surfaces at high tool feed rates (Figs. 4(a) and (b)), indicating a partially brittle response of the material. In addition, as the tool feed rate decreased, the period of the lamellar structure and the chip thickness also decreased. Fig. 5 is a higher magnification SEM image of the chip shown in Fig. 4(d).

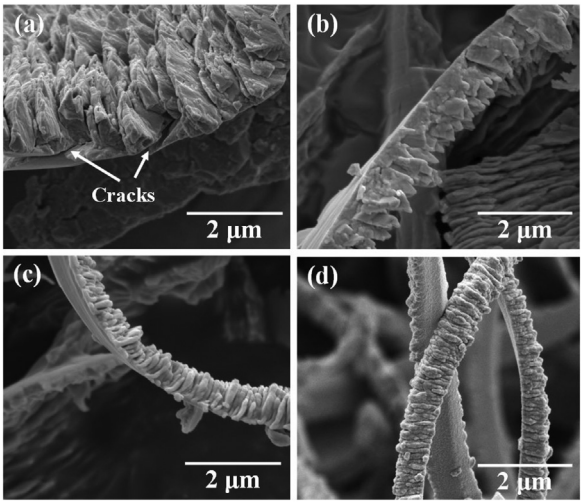

Fig. 4. SEM images of cutting chips obtained when: (a) $f = 10$, (b) $f = 5$, (c) $f = 2$, and (d) $f = 0.5\,\mu$m/rev.

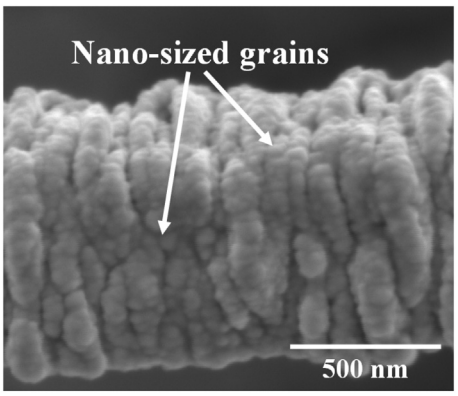

Fig. 5. High-magnification SEM image of a cutting chip obtained at $f = 0.5\,\mu$m/rev, which is composed of extremely fine grains.

The entire chip seems to be composed of fine grains, the sizes of which are ~50 nm. Such granular chip morphology was rarely reported in metal cutting. Moreover, the grain size is distinctly smaller than that of the raw material before cutting (~300 nm), indicating that grain refinement is very significant in the cutting process of Y-TZP.

3.3. Raman spectroscopy

To investigate possible phase transformations of the workpiece material caused by cutting, laser micro-Raman spectroscopy was used. Typical Raman spectra of the machined surface and the cutting chips are shown in Figs. 6 and 7, respectively. In Fig. 6, tetragonal (T) peaks dominate all the spectra, indicating that the phase transformation in the workpiece is minimal. In Fig. 7, however, monoclinic (M) peaks at 185 cm^{-1} become stronger, indicating that significant tetragonal-to-monoclinic phase transformation occurs during chip formation.

In order to quantify the extent of the phase transformation, the intensity ratio of the monoclinic phase, X_m, was calculated using

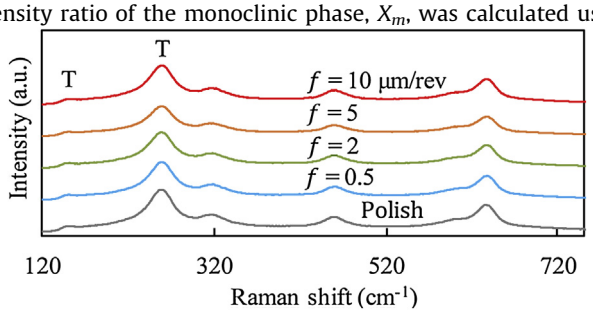

Fig. 6. Raman spectra of surfaces machined at different tool feed rates.

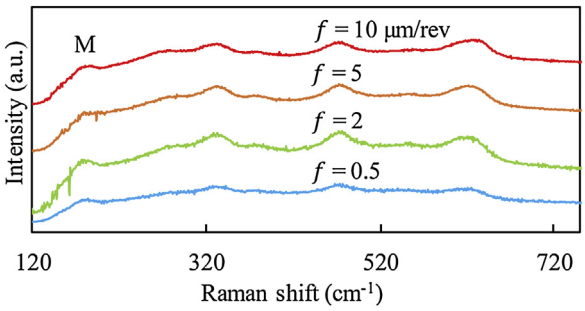

Fig. 7. Raman spectra of chips obtained at different tool feed rates.

Eq. (2), as follows [5]:

$$X_m = \frac{I_m(181) + I_m(190)}{0.33 \times (I_t(147) + I_t(265)) + I_m(181) + I_m(190)} \quad (2)$$

where I_m and I_t refer to the intensities of the monoclinic and tetragonal peaks, respectively, in the Raman spectra. Fig. 8 shows the change in X_m for the machined surface. X_m increases as the tool feed rate increases, and reaches a maximum at f=5 μm/rev. Further increase of tool feed rate causes a slight decrease in X_m, due to the occurrence of brittle fractures. From the trend of X_m shown in Fig. 8 and that of surface roughness in Fig. 3, it is illustrated that both the surface roughness and the subsurface phase transformation are low, i.e., the surface integrity is high [6], at a low tool feed rate (0.5 μm/rev).

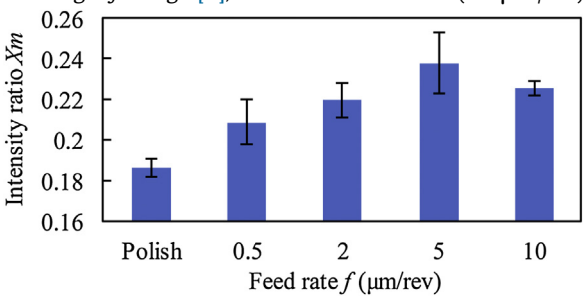

Fig. 8. Intensity ratio of monoclinic phase in surfaces machined at different tool feed rates.

3.4. Cross-sectional TEM observation

To further examine the subsurface layer of the machined workpiece, transmission electron microscopy (TEM) observation was performed. The TEM samples were cut from different machined areas and thinned to ~100 nm using focused ion beam techniques to enable electron transmission. Fig. 9(a) shows the TEM image of a region machined at f=5 μm/rev. A crack is observed at a depth of ~500 nm from the surface, above which is a region of refined grains. Fig. 9(b) is a TEM image of a region machined at f=0.5 μm/rev. In this region, no crack is observed. A layer of ultra-fine grains is seen below the surface. The grain size is tens of nanometres, similar to that in cutting chips (Fig. 5). Grain refinement improves the mechanical properties of the surface.

3.5. Cutting force

Fig. 10 shows the results of the cutting force measurement during machining. Both the principal force F_c and thrust force F_t increase drastically as the tool feed rate is increased from 0.5 to 2 μm/rev, and then increase gradually with a further increase in the tool feed rate. It is noteworthy that F_t is larger than F_c through all the experiments. This was due to the negative effective rake angle induced by the tool edge radius at micro-nanometre scale cutting.

3.6. Tool wear

The tool edge was observed using SEM after cutting tests for a total cutting distance of 62 m. Fig. 11 shows SEM images of the tool

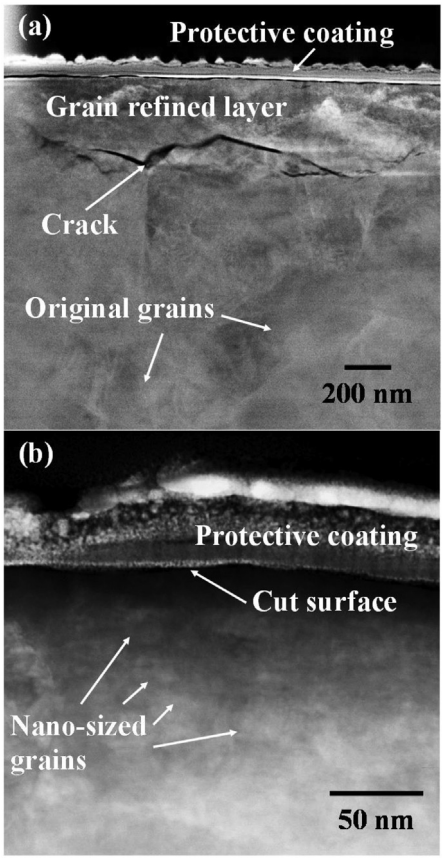

Fig. 9. Cross-sectional TEM images of regions cut at feed rates of (a) 5 and (b) 0.5 μm/rev.

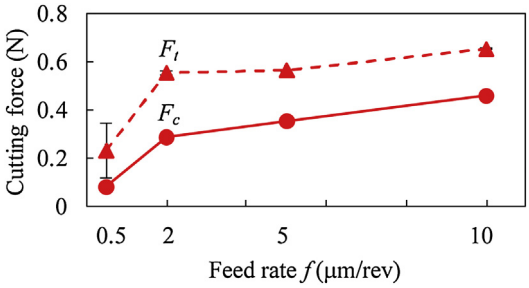

Fig. 10. Change in cutting force with tool feed rate.

edge. Crater wear, flank wear, and material adhesion were observed along the edge of the tool. The wear pattern of the tool edge shown in Fig. 11(b) (correspondingto the right side of the shoulder region in Fig. 1) was not uniform, with regions of deeper and wider crater wear as well as wavy flank wear. This was caused by the abrasive scratching effect of the coarse grains of the workpiece material at large undeformed chip thicknesses. In contrast, in Fig. 11(c) (correspondingto the left side of the shoulder region in Fig. 1), the crater wear is very narrow and the flank wear region is smooth. This is the result of uniform friction between the

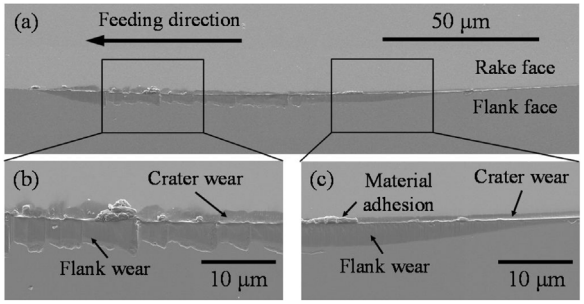

Fig. 11. SEM images of tool edge after cutting: (a) general view, (b) close-up view of left side, (c) close-up view of right side.

tool and the workpiece with refined grains at a nanometre scale undeformed chip thickness.

4. Discussion

Severe plastic deformation (SPD), which generates large plastic strains in bulk materials, is a well-known method for producing ultra-fine-grained metals [7]. The grain refinement during SPD is the result of the formation of new grain boundaries due to motion of dislocations, triggered by large plastic strains [8]. In ultraprecision cutting, the shear deformation occurring at the shear zone is a kind of SPD, which may have facilitated grain refinement in the chip formation process. The mechanism of chip formation in Y-TZP is schematically shown in Fig. 12.

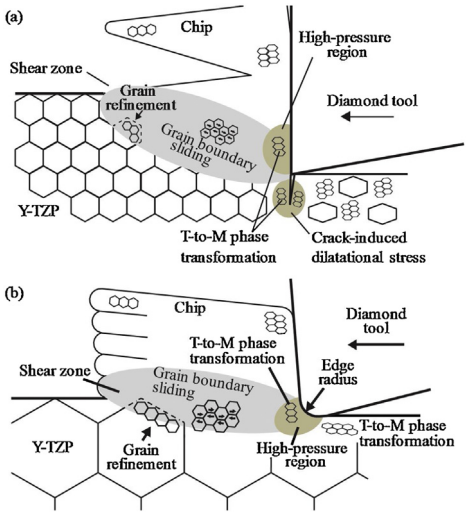

Fig. 12. Schematic model for chip formation in Y-TZP at (a) large and (b) small undeformed chip thicknesses.

Normally, Y-TZP is a brittle material and dislocations do not propagate at room temperature due to strong ionic or covalent bonds [9]. However, grain boundary sliding occurs easily in Y-TZP as the grain size becomes smaller [10]. It is found that dislocation motion and ultra-fine grains could be achieved in Y-TZP by high-pressure torsion [9]. From these reports, it can be said that grain refinement occurs in the ultraprecision cutting of Y-TZP by large plastic strain at the shear deformation zones. These refined grains can move due to grain boundary sliding, which is similar to dislocation movement in metals [10]. This mechanism yields plastic deformation macroscopically and forms continuous chips with a lamellar structure, as schematically shown in Fig. 12.

At large undeformed chip thicknesses, as shown in Fig. 12(a), cracks occur due to the tensile stress near the tool tip. These cracks propagate along the grain boundaries, causing microfractures and grain dislodgements. However, further crack propagation is prevented by a dilatational stress-induced T-to-M (tetragonal-to-monoclinic) phase transformation around the crack tip. This stress-induced toughening mechanism leads to Y-TZP's high fracture toughness [11]. As a result, the microfractures in Y-TZP cutting is distinctly smaller than those in cutting single crystals such as Si and Ge. At the same time, a high-pressure region forms in front of the tool tip, which also causes tetragonal-to-monoclinic phase transformation [12], as shown in Fig. 12(a). At small undeformed chip thicknesses, however, the tool edge radius is relatively large, and the effective rake angle is negative, creating high pressure in front of the tool tip, as shown in Fig. 12 (b). This local high pressure not only prevents crack generation but also causes tetragonal-to-monoclinic phase transformation.

To investigate the pressure distribution during Y-TZP cutting, FE analysis was performed by using an FE simulation program AdvantEdge (Third Wave Systems, USA). The tool shape and cutting parameters used in the simulation were the same as those used in the experiments. The pressure-sensitive Drucker-Prager constitutive model [13] was adopted to define the material property for Y-TZP. Fig. 13 shows pressure distributions in the cutting area at various undeformed chip thicknesses. The pressure in front of the tool tip is beyond 12 GPa, which is high enough to induce a tetragonal-to-monoclinic phase transformation [12].

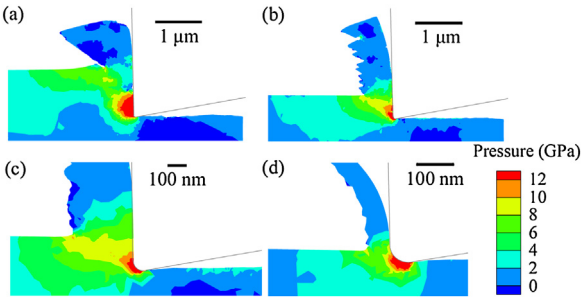

Fig. 13. Pressure distributions in the cutting area: (a) $h = 1000$, (b) $h = 500$, (c) $h = 200$, (d) $h = 50$ nm.

5. Conclusions

Y-TZP was cut by a single-crystal diamond tool, and a smooth surface of 5 nm Sa was obtained at a low tool feed rate. At a high feed rate, however, surface and subsurface microfractures occurred. Two mechanisms dominating the material removal were identified. A high-pressure-induced tetragonal-to-monoclinic phase transformation was detected in both the machined surface and the cutting chips by Raman spectroscopy, with the monoclinic intensity ratio increasing as the tool feed rate increased. Cross-sectional TEM observation revealed that 10 nm-sized fine grains, generated by large-strain shear deformation, dominated both cutting chips and the subsurface layer of the workpiece. The grain refinement phenomenon facilitated plastic flow and continuous chip formation as well as improved surface integrity. This study has thus demonstrated the possibility of the direct fabrication of small 3D Y-TZP parts such as dental implants by ultraprecision cutting or end milling using single-crystal diamond tools.

References

[1] Krishnamurthy R, Arunachalam LM, Gokularathnam CV, Venkatesh VC (1991) Grinding of Transformation-Toughened Y-TZP Ceramics. *CIRP Annals – Manufacturing Technology* 40(1):331–333.
[2] Peters DW, Bourret ED, Power MP, Arnold J (2013) High Performance Grinding of Zirconium Oxide (ZrO_2) Using Hybrid Bond Diamond Tools. *CIRP Annals – Manufacturing Technology* 62(1):343–346.
[3] Uehara K, Takeshita H (1986) Cutting Ceramics with a Technique of Hot Machining. *CIRP Annals – Manufacturing Technology* 35(1):55–58.
[4] Kizaki T, Harada K, Mitsuishi M (2014) Efficient and Precise Cutting of Zirconia Ceramics Using Heated Cutting Tool. *CIRP Annals – Manufacturing Technology* 63(1):105–108.
[5] Muñoz Tabares JA, Anglada MJ (2010) Quantitative Analysis of Monoclinic Phase in 3Y-TZP by Raman Spectroscopy. *Journal of the American Ceramic Society* 93(6):1790–1795.
[6] Jawahir IS, Brinksmeier E, M'Saoubi R, Aspinwall DK, Outeiro JC, Meyer D, Umbrello D, Jayal AD (2011) Surface Integrity in Material Removal Processes: Recent Advances. *CIRP Annals – Manufacturing Technology* 60(2):603–626.
[7] Brown TL, Swaminathan S, Chandrasekar S, Compton WD, King AH, Trumble KP (2002) Low-Cost Manufacturing Process for Nanostructured Metals and Alloys. *Journal of Materials Research* 17(10):2484–2488.
[8] Hansen N, Jensen DJ (1999) Development of Microstructure in FCC Metals during Cold Work. *The Royal Society* 357(1756):1447–1469.
[9] Edalati K, Toh S, Ikoma Y, Horita Z (2011) Plastic Deformation and Allotropic Phase Transformations in Zirconia Ceramics during High-Pressure Torsion. *Scripta Materialia* 65(11):974–977.
[10] Retamal C, Lagos M, Moshtaghioun BM, Cumbrera FL, Domínguez-Rodríguez A, Gómez-García D (2016) A New Approach to the Grain-Size Dependent Transition of Stress Exponents in Yttria Tetragonal Zirconia Polycrystals. The Theoretical Limit for Superplasticity in Ceramics. *Ceramics International* 42 (4):4918–4923.
[11] Evans AG (1990) Perspectives on the Development of High-Toughness Ceramics. *Journal of American Ceramic Society* 73(2):187–206.
[12] Gaillard Y, Anglada M, Jiménez-Piqué E (2009) Nanoindentation of Yttria-Doped Zirconia: Effect of Crystallographic Structure on Deformation Mechanisms. *Journal of Materials Research* 24(3):719–727.
[13] Feng L, Kang Y, Zhang G, Wang S (2010) Mechanism-Based Strain Gradient Drucker–Prager Elastoplasticity for Pressure-Sensitive Materials. *International Journal of Solids and Structures* 47(20):2693–2705.